**Estimation of Effective Permeability of Canadian Shield Granite Using Physics-Informed Neural Networks (PINN)**

Qingjun Bao [a], Zhenze Li [b]

a: Independent AI researcher, Brossard, Quebec, Canada

b: ERAD, Canadian Nuclear Safety Commission, 280 Slater, Ottawa, Ontario, Canada

**Abstract:** The recent rapid advancements in AI and machine learning have led to the development of innovative tools and strategies for numerical modeling that uses neural networks. Among these, the Physics-Informed Neural Network (PINN) has demonstrated its versatility and huge potential as a novel modeling approach. PINN incorporates physical constraints—such as Darcy's law and the continuity equation—along with initial and boundary conditions into the neural network's training process. Through this integration, the PINN approach reconstructs governing equations and is trained to compute solutions. Compared to traditional techniques like the Finite Element Method (FEM), PINN offers significant advantages in handling sparse datasets, solving inverse problems, and quantifying uncertainties.

This study applies the PINN methodology to estimate the effective permeability of intact granite samples from the eastern and western regions of the Canadian Shield (Stanstead and Lac du Bonnet). Through comparative analysis, the PINN model predicts the geometric mean effective permeability for Stanstead and Lac du Bonnet granite at $59.1 \times 10^{-19}$ m² and $1.08 \times 10^{-19}$ m², respectively. These results align closely with previous studies ($59.3 \times 10^{-19}$ m² and $1.09 \times 10^{-19}$ m²), confirming the reliability of the PINN method. Notably, the PINN approach provides continuous permeability field distributions, as well as the spatial variability of permeability within the granite. Furthermore, two successive benchmark models—one for consolidation and another for the unsaturated flow governed by Richards' equation—were analyzed using both the FEM and PINN. These investigations clearly validate the accuracy and consistency of the PINN model. In conclusion, this research demonstrates the applicability, potential, and prospect of a novel numerical toolset of PINN for evaluating the Multiphysics coupled processes encountered in deep geological environment.

Key words:

PINN, permeability, neural network, granite, FEM, simulation

# 1. Introduction

Deep geological disposal is internationally recognized as a sound and feasible approach for the long-term management of high-level radioactive waste. The fundamental objective of DGR is to ensure the effective isolation of radionuclides from the biosphere over timescales of up to millions of years. A critical determinant of the long-term safety and performance of geological repositories is the hydrogeological behavior of the host rock, among which permeability serves as a key parameter governing groundwater flow and the potential for radionuclide transport. Granite formations,

particularly those within tectonically stable environments such as the Canadian Shield, have been extensively investigated as potential host media due to their low intrinsic permeability, geochemical stability, and mechanical integrity over geological timescales [1, 2].

In line with international guidelines, including those established by the International Atomic Energy Agency (IAEA), the design and licensing of geological repositories require rigorous site characterization procedures [3]. These include detailed assessments of rock permeability and its spatial heterogeneity, as these parameters directly influence the flow paths and velocities of subsurface fluids. In low-permeability formations such as granite, groundwater movement is primarily governed by Darcy's law, which relates fluid flux to pressure gradients and intrinsic permeability of the medium. While granite is often treated as a homogeneous and isotropic medium in many models, this simplification may prove inadequate when addressing processes such as multiphase flow, gas transport, or localized fracture-dominated seepage, wherein spatial variability must be explicitly represented to ensure predictive accuracy.

Conventional methodologies for estimating effective permeability in crystalline rock typically rely on sparse in-situ measurements and geostatistical interpolation techniques, such as kriging. Although these methods have been widely adopted, they are constrained by several inherent limitations. First, the acquisition of high-resolution field data is both time-consuming and cost-intensive [4]. Second, interpolation techniques are not governed by physical laws and may result in permeability distributions that are inconsistent with fundamental flow principles [5]. Third, such approaches pose significant challenges for uncertainty quantification [6], particularly in extrapolating localized observations to repository-scale models, which are essential for performance assessment over long timescales.

Recent advances in scientific computing have introduced physics-informed neural networks (PINNs) as a promising framework for modeling subsurface flow in complex and data-scarce environments [7-9]. Unlike traditional numerical solvers, PINNs incorporate governing equations—such as Darcy's law and mass conservation—directly into the loss function of the neural network, which helps ensure that predicted solutions remain physically consistent [10], even in the presence of sparse or noisy datasets [11]. Moreover, the incorporation of Bayesian frameworks within PINNs facilitates uncertainty quantification, providing probabilistic estimates of key parameters such as permeability [12]. These features make PINNs particularly well-suited for characterizing heterogeneous geological formations, where data availability is limited but the underlying physics are well understood.

The integration of machine learning techniques into geoscientific modeling has gained substantial interest in recent years. Notably, graph neural networks have been employed to resolve fracture-controlled permeability by capturing complex topological structures often missed by continuum approaches [13]. Additionally, hybrid numerical schemes combining PINNs with finite element methods have demonstrated success in modeling coupled thermo-hydro-mechanical processes [14], which are central to understanding the evolution of repository systems under coupled influences from multiple loadings. These developments indicate the growing potential of physics-informed machine learning to address long-standing challenges in the field of geological disposal.

Building on these advances, the present study proposes a PINN-based framework for estimating the effective permeability of granite relevant to deep geological repositories. The framework was developed and validated using experimental data obtained from granite samples originating from the Canadian Shield, as reported by Selvadurai et al. [15]. In the original investigation, permeability fields were inferred using conventional interpolation methods such as kriging [15]. In contrast, the current study aims to test

the hypothesis that physics-informed neural networks offer a mesh-free, physically consistent, and data-efficient alternative for subsurface flow modeling. By directly embedding governing equations into the learning process, the proposed approach seeks to overcome the limitations of traditional methods and to improve the robustness of permeability estimation for safety assessments in nuclear waste repository design. The advantage of PINN was further demonstrated by two benchmark study cases that simulated classical Terzaghi's consolidation problem and unsaturated flow by Richards' equation.

## 2. Experimental Data and Sample Characterization

The experimental dataset used in this study originates from the work of Selvadurai et al. [15], who investigated two granite samples from geologically distinct regions of the Canadian Shield. Specifically, the Stanstead granite was obtained from the eastern part of the Shield, while the Lac du Bonnet granite came from the western region in Province of Manitoba. These two samples are representative of low-permeability crystalline rocks that exhibit spatial variability in permeability due to the presence of microfractures, mineralogical differences, and small-scale structural features.

Permeability measurements were carried out using a microscale permeameter on cubic specimens, with data collected on all six surfaces of each sample. For each surface, nine measurement points were recorded, resulting in a total of 54 data points per sample. The transient pulse decay method was used for testing, as it is particularly well-suited for low-permeability materials given its sensitivity to small pressure variations. The permeameter employed had an inner diameter of 25.4 mm and an outer diameter of 101.6 mm, operating under a constant applied pressure of 200 kPa. The resulting dataset captures the microscale heterogeneity in permeability and serves as the ground truth for training and validating the PINN framework.

The two granite types were reported to differ significantly in their geological histories and microstructural characteristics, which in turn influence their permeability behavior. The Stanstead granite exhibits a relatively homogeneous mineral composition, leading to more uniform permeability values, whereas the Lac du Bonnet granite displays a higher degree of microfracturing, resulting in more pronounced spatial variability. The contrasts in matrix properties make the dataset particularly valuable for testing the generalization capability of the PINN model across different forms of heterogeneity in crystalline rock.

## 3. Theories and methods

3.1. Physical Background and Governing Equations

Groundwater flow in low-permeability granite can be described by Darcy's law. When combined with the continuity equation, the governing equation for steady-state flow is expressed as:

$$\nabla(K\nabla p) = 0$$

where:

- K: Permeability tensor (m²)

- p: Pressure field (Pa)

In isotropic media, the permeability tensor simplifies to a scalar value ($K$). This study specifically focuses on the steady-state seepage problem under saturated flow conditions.

3.2. Experimental Data and Sample Description

This study utilizes experimental data provided by Selvadurai et al. [15], focusing on two granite samples originating from different regions of the Canadian Shield: the Stanstead granite from the eastern Shield and the Lac du Bonnet granite from the western Shield. Below are the key details of the samples:

Each sample underwent measurements using a microscale permeameter on all six surfaces. For each surface, nine data points were recorded, resulting in a total of 54 data points per sample. The measurements were conducted using the transient pulse decay technique. The equipment had an inner diameter of 25.4 mm, an outer diameter of 101.6 mm, and operated under an applied pressure of 200 kPa.

3.3. Physics-Informed Neural Network (PINN) Model

The setup of a PINN starts with the explicit definition of the partial differential equations (PDEs) that govern the physical problem under consideration, along with the specification of relevant boundary and initial conditions. Subsequently, a suitable neural network architecture is selected, such as a fully connected network or convolutional neural network, and its hyperparameters, including depth, layer width, and activation functions, are determined. The neural network's output is then differentiated with respect to its inputs via automatic differentiation, enabling the construction of a loss function that incorporates these derivatives into the PDEs. This loss function typically comprises PDE residual terms, boundary condition terms, and potentially data-fitting terms, which collectively facilitate the neural network's learning of a solution that approximates the governing equations of the physical system and its constraints. Through an optimization algorithm, such as Adam or L-BFGS, the network weights are updated to minimize the loss function, thereby driving the neural network's convergence towards an accurate representation of the physical system. The selection of hyperparameters, including learning rate, batch size, and training iterations, plays a crucial role in ensuring the network's convergence and accuracy.

3.3.1 Network Architecture

The PINN model constructed in this study consists of the following components:

- Input Layer: Accepts three-dimensional spatial coordinates ($x, y, z$).
- Feature Extraction Network: Composed of six hidden layers, each featuring 128 neurons and employing the tanh activation function for processing.
- Dual Output Heads: One branch predicts the pressure field ($p(x, y, z)$), while the other estimates the logarithmic permeability field ($\log K(x, y, z)$).

The choice to predict logarithmic permeability rather than directly predicting permeability ensures that the permeability values remain strictly positive and can handle variations across multiple orders of magnitude.

The network model is implemented using the PyTorch framework [16], with its complete mathematical representation provided as below:

$$h_0 = [x, y, z]$$

$$h_i = \tanh(W_i h_{i-1} + b_i), \qquad i = 1, 2, \ldots, 6$$

$$p = W_p \tanh(W_{p1} h_6 + b_{p1}) + b_p$$

$$\log K = W_k \tanh(W_{k1} h_6 + b_{k1}) + b_k$$

$$K = \exp(\log K)$$

where W and b represent the weight matrix and bias vector, respectively.

3.3.2 Loss Function Design

The core of the PINN method is integrating physical laws as constraints into the training process of the neural network. In this study, the design of the loss function consists of the following four components:

- Data Loss: Ensures the predicted permeability matches the surface measurement values, formulated as:

$$L_{data} = \frac{1}{N_d} \sum_{i=1}^{N_d} \left[ \log K_{pred}(x_i) - \log K_{mean}(x_i) \right]^2$$

This part aligns the model's predictions with the observational data, reducing the error in permeability estimations.

- PDE Loss: The PDE loss function, denoted as L_PDE, plays a crucial role in ensuring the physical consistency of the model by enforcing that the predicted pressure field and permeability field satisfy the fundamental governing equations of fluid flow in porous media—specifically, Darcy's law and the continuity equation. This is achieved by minimizing the PDE residual, which is calculated as the squared difference between the predicted and expected values of the divergence of the flux field.

Mathematically, the PDE loss function can be expressed as

$$L_{PDE} = \frac{1}{N_c} \sum_{i=1}^{N_c} \left[ \nabla \left( K_{pred}(x_i) \nabla p_{pred}(x_i) \right) \right]^2$$

where N_c represents the number of collocation points, x_i denotes the spatial coordinates of the i-th collocation point, K_pred(x_i) is the predicted permeability field at x_i, and p_pred(x_i) is the predicted pressure field at x_i.

The physical significance of this loss function lies in its ability to enforce momentum conservation in the predicted flow field. Darcy's law, which relates fluid flux to the pressure gradient and permeability, is a statement of momentum conservation. By minimizing the PDE loss function, the model is encouraged to produce predictions that satisfy these fundamental physical principles.

In practice, the PDE loss function is typically computed using automatic differentiation, which allows for the efficient calculation of the derivatives of the predicted pressure and permeability fields with respect

to the spatial coordinates. This can be accomplished using libraries such as TensorFlow or PyTorch, which provide built-in support for automatic differentiation.

The use of the PDE loss function offers several benefits, including the incorporation of prior knowledge about the physical system into the training process, regularization of the model to prevent overfitting, and the ability to learn from the underlying physics of the system. However, the PDE loss function may also introduce additional challenges, such as the need to carefully select collocation points and determine the weighting of the PDE loss term in the overall loss function.

To address these challenges, various techniques can be employed, such as the use of adaptive collocation points, which can be adjusted during training to focus on regions of high error, or the use of physics-informed neural network architectures, which can be designed to inherently satisfy the governing equations. Additionally, the PDE loss function can be modified or extended to accommodate more complex physics or additional constraints, such as nonlinear effects or constraints on the predicted flux or pressure fields.

The interplay between the PDE loss term and other loss terms in the overall loss function is also critical in determining the model's performance. For example, the weighting of the PDE loss term relative to the data-fitting term can significantly impact the model's accuracy and robustness. A high weighting of the PDE loss term may result in a model that is overly constrained by the physics, while a low weighting may lead to a model that is excessively influenced by the data. As such, the PDE loss constraint guarantees the physical consistency of the model by seamlessly integrating the governing equations into the training process.

- Boundary Loss: Ensures that boundary conditions are met and that the permeability field transitions smoothly at the boundaries:

$$L_{BC} = \frac{1}{N_b} \sum_{i=1}^{N_b} \left[ \log K_{pred}(x_i) - \log K_{mean}(x_j) \right]^2$$

where (x_j) represents the neighboring point of (x_i). This term enforces smooth boundary behavior and prevents abrupt transitions.

- Regularization Loss: Mitigates overfitting by penalizing large values of model parameters:

$$L_{reg} = \sum_{\theta \in \Theta} \theta^2$$

where $\Theta$ encompasses all parameters of the model. This term ensures the model's generalizability by discouraging overly complex parameter configurations.

The total loss function is a weighted sum of the above components:

$$L_{total} = w_{data} L_{data} + w_{PDE} L_{PDE} + w_{BC} L_{BC} + w_{reg} L_{reg}$$

In this study, the weights used are: $w_{data}$ = 10.0, $w_{PDE}$=$w_{BC}$=1.0, $w_{reg}$=0.01.

By carefully tuning these weights, the model balances data accuracy with physical fidelity and generalization, effectively addressing the challenges of training PINNs for complex problems.

3.3.3 Training Strategy

The model employs a two-phase optimization strategy to ensure efficient and accurate training.

Phase 1: Adam Optimization

In the first phase, the Adam optimizer is used for 50,000 iterations with a learning rate (LR) of 0.001 and a decay schedule. This approach enables rapid convergence in the early stages of training and avoids getting stuck in local optima.

Phase 2: L-BFGS Optimization

In the second phase, the L-BFGS optimizer is used for 500 refinement steps to further improve the model's accuracy and stability. The L-BFGS optimizer is a quasi-Newton method that performs a more refined search near the local optimum.

To enhance training efficiency and accuracy, several techniques are employed:

> Adaptive Learning Rate: The learning rate is dynamically adjusted based on the loss function's behavior during training to ensure convergence to the optimal solution.

> Checkpointing: Model parameters are periodically saved during training to allow for recovery to previous checkpoints in case of issues.

> Batch Training: The training data is divided into small batches (1024 points per batch) to reduce memory usage and increase training speed.

The combination of these techniques ensures that the model converges efficiently and stably to the optimal solution during training.


3.4. Effective Permeability Prediction

The calculation of effective permeability for granite samples is based on Darcy's law at the macroscopic scale. To evaluate the effective permeability in any given direction (e.g., the x-direction), the calculation process can be summarized as follows:

The mathematical expression for the x-direction is as follows:

$$K_{e,x} = \frac{1}{n^2} \sum_{i=1}^{n} \sum_{j=1}^{n} \left( \frac{n}{\sum_{k=1}^{n} 1/K(x_k, y_i, z_j)} \right)$$

Similarly, the effective permeability in the y-direction and z-direction can be determined using the same method. The geometric mean effective permeability of the sample is then defined as:

$$K_{geo} = \sqrt[3]{K_{e,x} K_{e,y} K_{e,z}}$$

In this study, n=31 is chosen to ensure accuracy, meaning that 31 evenly spaced points are selected in each direction for the calculations.

We then compared the PINN approach with the FEM/FDM methods combined with kriging interpolation used by Selvadurai et al. [15], by evaluating the modelling results of effective permeability. The factors including differences in data requirements, computational efficiency and handling of physical constraints and uncertainty were also briefly discussed.

## 4. Results and discussion

### 4.1. Model Training and Convergence Analysis

The PINN model successfully converged after 50,000 training iterations. Figure 1 illustrates the evolution of the total loss and its individual components throughout the training process. The loss curves reveal three distinct phases: (1) a rapid decline in the first 5,000 iterations, where the total loss dropped from an initial magnitude of $10^2$ to nearly $10^{-1}$; (2) a gradual reduction between 5,000 and 25,000 iterations; and (3) stabilization beyond 25,000 iterations, indicating successful convergence.

A detailed breakdown of the loss components shows that the Data Loss eventually settled around $10^{-1}$, while the PDE Loss decreased sharply to an extremely low value (below $10^{-30}$), confirming that the model effectively satisfied the underlying physical constraints. The Boundary Loss exhibited a significant drop after approximately 5,000 iterations, whereas the Regularization Loss (Reg Loss) remained stable at a magnitude of $10^0$, as expected. These observations demonstrate that the PINN model effectively balanced data fitting and physical consistency, ultimately achieving a physically plausible reconstruction of the permeability field.
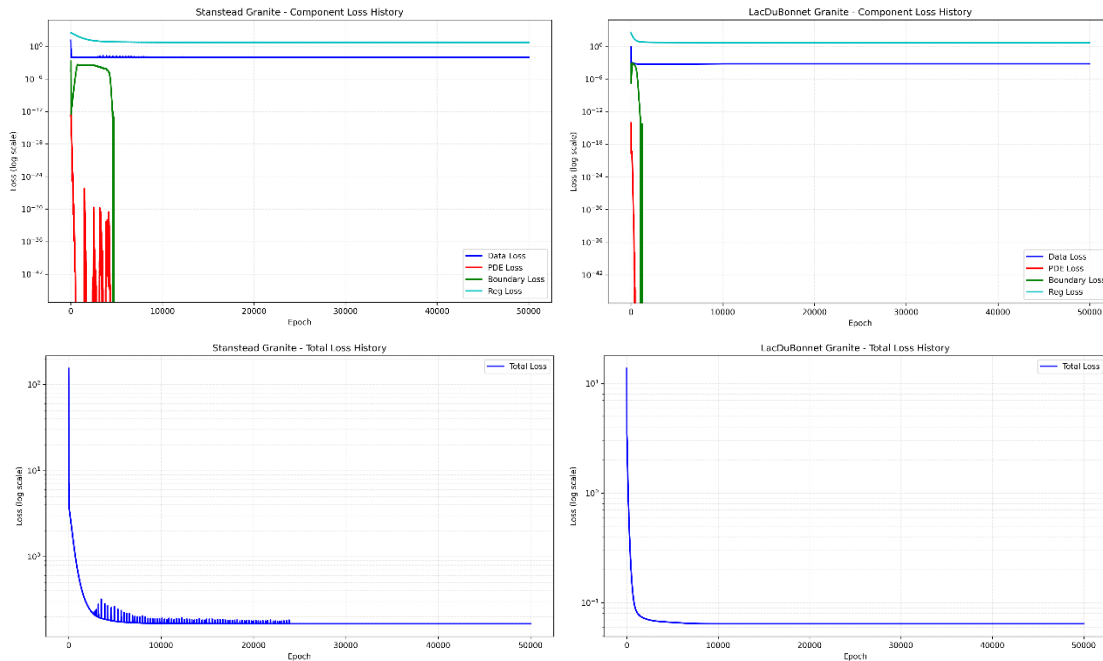


Figure 1  Evolution of training loss with training epoch for Stanstead (left) and Lac Du Bonnet (right) samples

### 4.2. Spatial variability in permeability

Using the trained physics-informed neural network (PINN) model, we successfully reconstructed the three-dimensional permeability fields for two granite specimens. The permeability distribution patterns of Stanstead granite are visualized in Figures 2. Analysis of these permeability distribution maps reveals

several important characteristics. The Stanstead granite exhibits a remarkably homogeneous permeability field, with most measured values falling within the narrow range of 54-56×10⁻¹⁹m². Notably, the distributions display no significant anomalies or abrupt fluctuations, demonstrating the model's ability to produce physically realistic predictions. The high degree of similarity observed across all three orthogonal planes strongly reflects the isotropic nature of granite material. Furthermore, the permeability field maintains smooth and continuous spatial transitions, a feature that aligns well with the known behavior of natural geological formations. These consistent patterns across different cross-sectional views validate both the reliability of our PINN model and the inherent material properties of the tested granite samples.

The reconstructed permeability fields show excellent agreement with expected geological characteristics, particularly in terms of spatial consistency and physical plausibility. The homogeneous distribution observed in Stanstead granite, combined with the absence of abnormal peaks or discontinuities, provides strong evidence for the model's accuracy in capturing the material's intrinsic permeability structure. This successful reconstruction demonstrates the effectiveness of our PINN approach in handling complex geophysical inverse problems while maintaining strict adherence to physical constraints. The results not only confirm the isotropic nature of the granite samples but also highlight the model's capability to produce geologically meaningful outputs without introducing artificial artifacts or unphysical features.
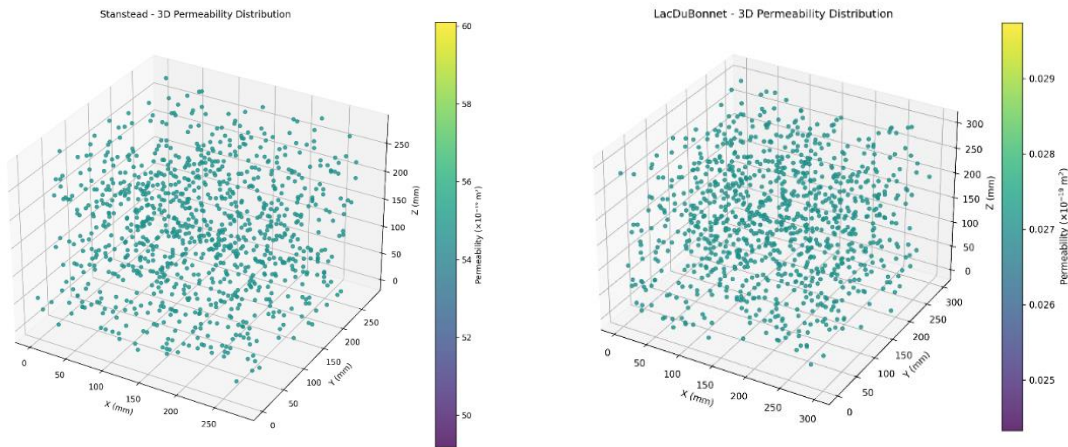


Figure 2  Spatial distribution of modelled permeability for Stanstead (left) and Lac Du Bonnet (right) samples[ZL1]

Figure 2 illustrates the three-dimensional permeability distribution of both Stanstead and Lac Du Bonnet granite sample, presented as a scatter plot. Each dot on the diagram represents a specific location within the rock, and the color of the dot indicates the permeability at that position. The color gradient ranges from purple, representing low permeability, to yellow, signifying high permeability. The cube-shaped sample has dimensions of approximately 280mm×280mm×280mm, with the permeability values predominantly falling within the range of 50–60 × 10⁻¹⁹ m². The scatter plot includes approximately 1,000 randomly distributed data points, and the majority of these points are displayed in cyan-green hues (about 54–56 × 10⁻¹⁹ m²), reflecting the uniformity of permeability across the sample.

Upon analyzing the permeability distribution of the Stanstead granite sample, several important observations can be made. Firstly, the permeability distribution appears highly uniform throughout the rock, with no distinct high-permeability or low-permeability regions. Most points on the diagram are concentrated in the cyan-green range (approximately $54$–$56 \times 10^{-19}$ m²), indicating the exceptional homogeneity of the sample. Secondly, the distribution exhibits isotropic characteristics, as there is no noticeable variation in permeability in different spatial directions, nor any evidence of directional preference. This demonstrates that Stanstead granite possesses remarkable isotropic properties.

Additionally, the permeability values remain stable, varying within a narrow range (primarily between $54$–$56 \times 10^{-19}$ m²), and the maximum deviation does not exceed 10% of the total range. This stability affirms the reliability of the PINN model's predictions. Furthermore, no anomalous regions are observed; extreme high or low values are absent, and there are no abrupt transitions in permeability. This suggests that the rock sample lacks large fractures or densely packed zones internally. Lastly, the boundary effects are negligible. Sampling points near the cube's boundaries show no systematic differences in permeability compared to internal points, highlighting the model's success in addressing boundary conditions.

The PINN model effectively reconstructed a three-dimensional permeability field for the Stanstead granite sample that is consistent with physical expectations. The model did not produce numerical artifacts or unrealistic results, demonstrating its applicability in geological permeability research. The stability and uniformity of the permeability distribution underscore Stanstead granite's predictability as a barrier material, making it advantageous for assessing the long-term safety of deep geological disposal repositories. Compared to traditional interpolation methods, the PINN approach reconstructs a three-dimensional permeability field that maintains physical consistency, and avoids potential non-physical oscillations or extreme values.

The permeability field of Lac du Bonnet granite exhibits several distinct characteristics. Firstly, its overall permeability is significantly lower than that of Stanstead granite, with most regions falling within the range of $0.9$–$1.2 \times 10^{-19}$ m². Secondly, the permeability distribution also demonstrates high uniformity and isotropy, like that of Stanstead granite. However, compared to Stanstead granite, Lac du Bonnet granite shows slightly higher spatial variability.

Statistical analyses reveal that the permeability distributions of both types of granite can be well-fitted using log-normal distributions, consistent with the typical characteristics of geological materials. The mean permeability of Stanstead granite is $55.3 \times 10^{-19}$ m², with a standard deviation of $1.7 \times 10^{-19}$ m², while Lac du Bonnet granite has a mean permeability of $1.05 \times 10^{-19}$ m² and a standard deviation of $0.12 \times 10^{-19}$ m².

### 4.3. Results of Effective Permeability Calculation

Based on the reconstructed three-dimensional permeability fields, effective permeability values were calculated for the two types of granite in three orthogonal directions, as well as the geometric mean effective permeability. Table 1 summarizes the results obtained using the PINN method and compares them with those reported value derived from traditional methods [15].

As shown in Table 1, the PINN method demonstrates high consistency with traditional methods, with a maximum relative error not exceeding 3%. Furthermore, the effective permeability ratio between the

two granites (Stanstead/Lac du Bonnet) calculated using the PINN method is 54.7, while the value derived from traditional methods is 54.4, yielding a relative error of only 0.55%. This indicates that the PINN method achieves comparable accuracy to traditional methods in estimating effective permeability.

Notably, the effective permeability values obtained by the PINN method are highly consistent across the three orthogonal directions. This reflects the isotropic nature of the granite, aligning with geological understanding. This observation highlights the PINN model's capability to accurately capture the physical properties of the rock.

Table 1  Permeability predictions by PINN and Kriging (X $10^{-19}$ m$^2$)

| Rock Type | Method | X Direction | Y Direction | Z Direction | Arithmetic Mean |
|---|---|---|---|---|---|
| | PINN | 59 | 59.3 | 59 | 59.1 |
| Stanstead | Traditional (Kriging) | 59.2 | 59.5 | 59.2 | 59.3 |
| | Relative Error (%) | -0.34% | -0.34% | -0.34% | -0.34% |
| | PINN | 1.09 | 1.08 | 1.07 | 1.08 |
| Lac du Bonnet | Traditional (Kriging) | 1.08 | 1.09 | 1.1 | 1.09 |
| | Relative Error (%) | 0.00% | 0.00% | -2.73% | -0.92% |

### 4.4. Comparison Analysis Between PINN and Traditional Methods

Compared to traditional methods such as FEM/FDM combined with kriging, the PINN approach exhibits significant advantages across various aspects, as detailed in Table 2. One major advantage is its data efficiency. The PINN method successfully reconstructed the entire three-dimensional permeability field using only 54 surface measurement points, whereas traditional methods typically require denser datasets or additional assumptions to achieve similar outcomes. This efficiency highlights PINN's capability to optimize data usage.

Additionally, PINN naturally excels at solving inverse problems, such as determining internal permeability distribution based on known surface measurements. Unlike traditional methods that rely on iterative techniques or regularization methods, PINN achieves this with ease, providing a seamless solution. The PINN approach also generates continuous permeability fields over the entire domain, allowing evaluation at any desired point without depending on grids or requiring interpolation. This eliminates the grid dependency observed in traditional methods.

Another noteworthy advantage is physical consistency. Loss function curves demonstrate that the PDE loss drops rapidly to very low values, indicating that the reconstructed permeability field satisfies Darcy's law and the continuity equation. This ensures that the model adheres to fundamental physical principles.

Furthermore, PINN's mesh-free nature eliminates the need for complex three-dimensional meshes, making it particularly well-suited for handling problems involving intricate geometries or multi-scale

features. PINN inherits the nature of neural network models that heavily rely on data. Although mesh is unnecessary, PINN creates colocation points within the domain to derive errors for training. This somewhat resembles the meshing indices widely adopted in FEM. The PINN framework also supports scalability, enabling easy extension to multi-physics coupling problems such as thermo-hydraulic-mechanical-chemical (THMC) coupling.

However, the PINN method also has limitations. The training for network is computationally intensive which requires adjustments to hyperparameters and may fail to find a universal solution when converge to local optimal solutions. Despite these challenges, the advantages of the PINN method (particularly its efficiency, versatility, and physical reliability) make it highly effective for estimating granite permeability in this study.

Table 2  Comparison of various features between PINN and FEM based approaches

| Characteristic | PINN Method | FEM based or Kriging Method |
|---|---|---|
| Data needs | Sparse | Dense |
| Solving | Optimizes neural network parameters to minimize loss residuals | Discretizes equations to solve linear system equations |
| Governing equations | Incorporated through loss function (soft constraint) | Strict discretization of equations (hard constraint) |
| Computational efficiency | Solving once, results inferred for re-analysis | Repeated solving for re-analysis |
| Continuity | Provides continuous solution over the entire domain | Provides solution on discrete gaussian points, requires interpolation in terms of shape function |
| Inverse problem | Can learn the inverse target parameters directly from the data and physics | Need multiple tries of different guesses until acceptable matches |
| Parameter scale | Amount of wights and biases is tied to number of neurons, stays constant once set up | Degree of freedom increases with meshing density |

## 5. PINN benchmark vs FEM

This section continues the verification by benchmarking the PINN with FEM results. The benchmark is undertaken for growingly complex problems, i.e. the 1D saturated consolidation and then the unsaturated flow.

### 5.1. 1D consolidation problem

Terzaghi's one-dimensional consolidation theory (1923) is a fundamental theoretical model in soil mechanics, describing the process of pore water drainage and effective stress increase in saturated clay under loading. Its core assumptions include: 1) one-dimensional drainage: soil compression and seepage occur only in the vertical direction; 2) Darcy's law: seepage velocity is proportional to the hydraulic gradient; 3) small-strain linear compression; 4) full saturation. The 1D consolidation equation can be given as:

$$\frac{\partial u}{\partial t} = c_v \frac{\partial^2 u}{\partial z^2}$$

where u is pore pressure, t is time, z is distance from drainage boundary, and $c_v$ is consolidation coefficient $c_v = k(1+e_0)/a_v\gamma_w$, with k as hydraulic conductivity, $a_v$ as compression index, and $\gamma_w$ is water density, $e_0$ is initial pore ratio.

This equation describes how pore pressure dissipates over time due to drainage, leading to soil settlement. The theory remains widely used in geotechnical engineering for predicting consolidation settlement in soft clay layers. It is also a typical diffusion equation, that shares the same formula with species diffusion and thermal transport. It serves a good example of benchmark for new numerical tools, such as PINN. Here we implement both PINN (self-developed python code) and FEM (by COMSOL) to solve the above equation, and make comparison of both results. The simulation case involves following parameters: thickness of porous media at 1 m, drainage boundaries for both ends, initial pore pressure is normalized to 1.0, and consolidation coefficient Cv=1.0.

## 5.2. Richards equation for unsaturated flow

The Richards equation, formulated by Richards in 1931, is a key model in hydrology for describing water movement through unsaturated porous media, such as soils and rocks. It integrates Darcy's law, which governs fluid flow in porous materials, with the principle of mass conservation to capture how water infiltrates and redistributes in these media. This nonlinear partial differential equation accounts for changing soil properties—like hydraulic conductivity and moisture retention—making it essential for studying the vadose zone, the unsaturated layer between the surface and groundwater. Its importance finds application in multiple fields: groundwater recharge, contaminant transport, drainage design and slope stability analysis. Though its nonlinearity and data demands pose computational challenges, the Richards equation remains a cornerstone in understanding unsaturated flow. Its classical form is written as

$$\frac{\partial \Theta}{\partial t} = \nabla\big(K(\nabla h + e_z)\big)$$

where olumetric water content, t is time, K is hydraulic conductivity, h is pressure head (in m $H_2O$, negative in unsaturated conditions), nit vector in vertical direction for gravity.

The volumetric water content can be represented by porosity multiplied by saturation degree, and is a function of pressure head. Such relationship can be represented by the known van Genuchten equation. Let $\alpha$ as air entry value and n=2, then the water retention curve for granite is given as

$$S_e = \frac{1}{\sqrt{1 + (\alpha h)^2}}$$

where $S_e$ is effective saturation degree in the form of $S_e = (\Theta - \Theta_r)/(\Theta_s - \Theta_r)$, with $\Theta_s$ and $\Theta_r$ as saturated and residual water content, respectively.

Vapor storage $C_m$ is written as

$$C_m = (\Theta_s - \Theta_r)\alpha n m \frac{S_e^{1+1/m}\left(1 - S_e^{1/m}\right)^{m+1}}{|h|}$$

where m=1-1/n.

By inserting the model parameters, it reduces to the form of

$$C_m = \alpha \rho g \frac{S_e^3 (1 - S_e^2)^{1.5}}{p}$$

Relative permeability of van Genuchten model gives a lower bound of the unsaturated permeability, as shown below

$$k_r = S_e{}^l \left[ 1 - \left( 1 - S_e^{1/m} \right)^m \right]^2$$

where l=0.5, and m=1-1/n=0.5.

Overall, the Richards equation is written as

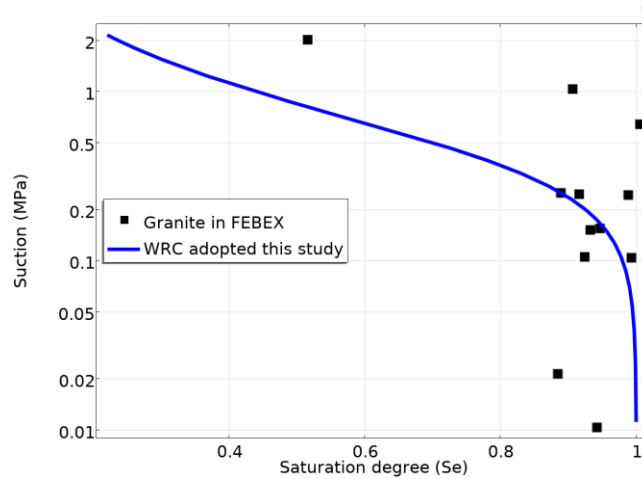$$(C_m + S_e S) \frac{\partial p}{\partial t} = \nabla \left[ \frac{\kappa_s k_r}{\mu} (\nabla p) \right]$$

Figure 3  Water retention properties of granite sample from FEBEX project [17] and its fitting with van Genuchten formula

We carried out a benchmarking study of the unsaturated flow from boundary inward the sample, with consideration of the reported experimental setup for granite specimen in [15]. The water retention curve of this sample was absent from original studies. We refer its characterization to a similar granite as shown in Fig. 3 that was investigated in FEBEX project [17]. The thickness of porous media is 0.1 m, saturated permeability is 1e-19 $m^2$, initial pore pressure is -2.0 bar, and boundary pore pressure is 1 bar. In order to relive the stress on the simulations, the boundary condition is gradually ramped from initial value to the final value of 1 bar. The compressibility of pore fluid and porous media is 4e-10 and 1e-7 $Pa^{-1}$, respectively. The simulation settings were identical for PINN and FEM models. Time is normalized to unit by divided with 5 days.

### 5.3. Results and discussion

Figures 4-5 show the results of the benchmark comparison of PINN and FEM, which indicate excellent agreement with each other. The training loss of the PINN consistently decreases and converges toward the exact solution. It is also noted that the learning curve flattens with additional training epochs,

suggesting that extended training may be required for improved accuracy. One interesting observation is that the PINN approximates the exact solution better in region of output that is away from 0. This is likely due to the loss function's reliance on mean squared error, which produces smaller gradients near zero, making it harder for the neural network to resolve small errors effectively [7, 10, 18]. Even for classical FEM,

From Figure 5, the pore pressure profile suggests the sample remains unsaturated even after 5 days of saturation. This study case was to demonstrate the accuracy of PINN vs FEM models. However, the slow saturation is attributed to the large compressibility value (1e-7 1/Pa) taken for the porous media adopted in the model.
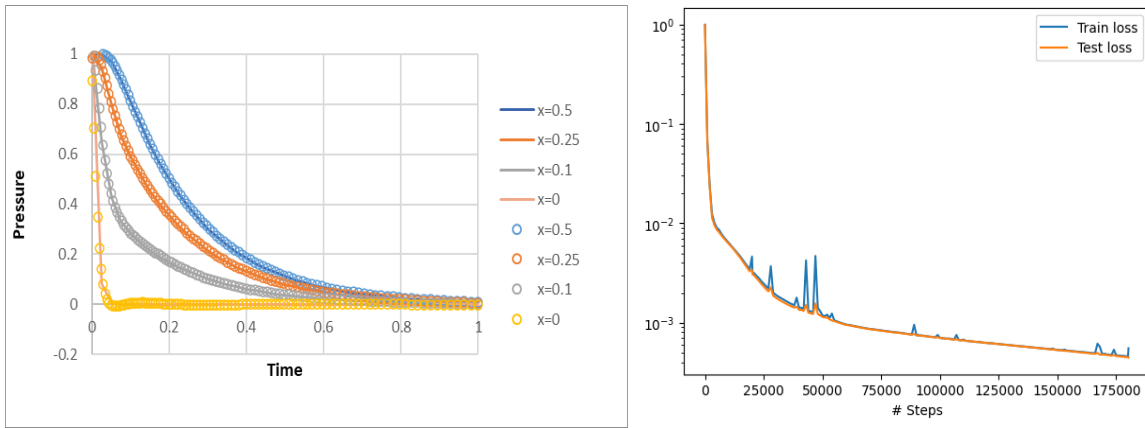


Figure 4  Pore pressure evolution with time for the 1D consolidation problem calculated by PINN vs FEM (left) and PINN training loss (right). Solid lines are obtained from FEM method while open symbols are from PINN approach.
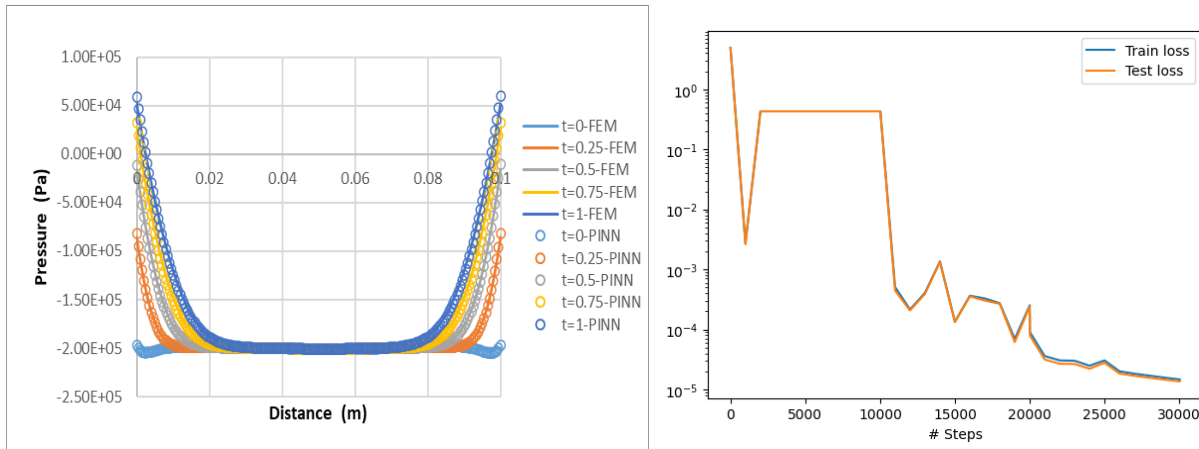


Figure 5  Pore pressure distribution at different time for the unsaturated flow problem of Richard's equation calculated by PINN vs FEM

### 5.4. Further discussion on variability of measured permeability

As indicated by [15] the measured permeability has been found to vary in an inconsistent way, which could experience both increasing and decreasing trend with elapsed time. Several factors were mentioned in

the original article. Here we attempted to illustrate the variability of measured flux (that is used to derive the permeability) as a function of unequilibrated distribution of pore pressure that can be resulted either from insufficient saturation or transient perturbation from adjacent measuring points. The simulations were conducted using COMSOL ver 5.3 [19]. The granite sample was 0.4X0.4 m$^2$ in dimension. The permeability of 1e-19 m$^2$ was applied, along with WRC parameters  determined by Figure 3. The initial pore pressure was taken as -2 bar that is around the air entry value. Saturation was accomplished by applying ambient atmospheric pressure on the outer boundary. Time dependent unsaturated flow with Richards' equation was simulated by COMSOL [19]. It has been reported that the specimen was confined under elevated stress (3 MPa). However, due to the increased complexity introduced by the inclusion of hydro-mechanical (HM) coupling, the effect of confinement loading was not considered in this study. This will be addressed in future work, once we are able to implement Physics-Informed Neural Networks (PINN) to solve such coupled problems.
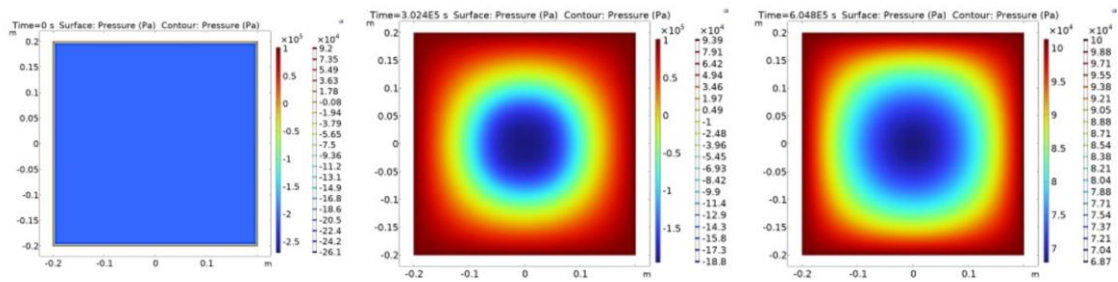


Figure 6  Pore pressure distribution in granite specimen at different saturation duration (0, 3.5, 7 days)
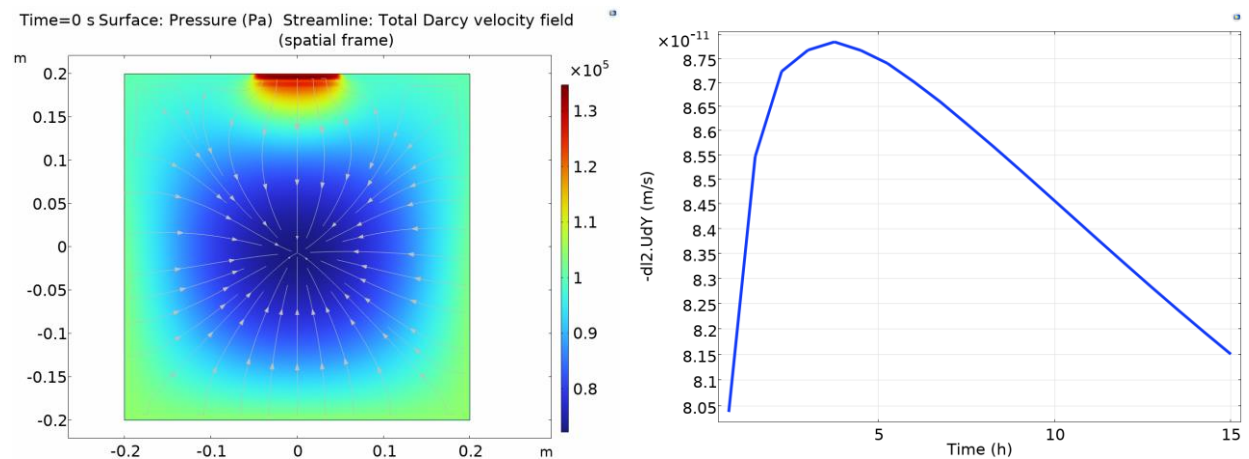


Figure 7  Animation of pore pressure evolution since permeability measurement commences at end of sample saturation (day 7) (left) and the simulated flow rate through the injection boundary as a function of elapsed time (right)

Figure 6 shows the pore pressure evolution during the simulated 7-day saturation process. At the end of the saturation phase, the pore pressure reaches its saturation state, but remains spatially heterogene-

ous. This indicates that the assumption of a uniform pore pressure distribution may not be valid for permeability calculations based on the micrometer injection test. Since the degree of confidence in this assumption is crucial, and to further investigate, the variability of injection flux was examined as an indicator of this heterogeneity.

Figures 7 show the results of subsequent application of injection pressure at the upper boundary. The left panel shows the pore pressure evolution, depicting the pressure distribution within the system at that time and the direction of fluid (or flux) flow (from high-pressure areas to low-pressure areas, converging towards the center). The right panel tracks the temporal evolution of the perpendicular flow rate at the injection boundary, which grows quickly at the beginning until it peaks at about 4-5 hours. The flow rate decreases afterwards, with an overall variability of approximately 10% of the average over the 15-hour duration. This clearly demonstrates the influence of unequilibrated pore pressure on the final result of the permeability measurement. Due to the low permeability, our model suggests a very slow process for the sample to reach a uniform pore pressure. Consistent with this observation, the estimated permeability varies with elapsed time, which is in agreement with experimental findings. Overall, the data variability is at an acceptable level of less than 10%. This further confirms the validity of the approach developed by [15].

## 6.  Conclusions

This study estimated the effective permeability of two Canadian Shield granites using a physics-informed neural network (PINN) method, showing good agreement with traditional finite element/finite difference methods combined with kriging. The PINN approach incorporated physical laws into network training, accurately reconstructing permeability fields and matching experimental data. The geometric mean permeabilities were consistent with traditional methods, with relative errors below 1%. Unlike conventional methods, PINN provided continuous permeability distributions, revealing spatial variability and isotropy. It offered advantages in data efficiency, inverse problem solving, continuous solution generation, and mesh-free operation, especially for complex geological problems with limited data. Statistical analysis confirmed log-normal permeability distributions for both granites, aligning with geological expectations and supporting the reliability of PINN results. Additionally, two benchmark models—one for consolidation and another for unsaturated flow governed by Richards' equation—were analyzed using both FEM and PINN. These tests confirmed the accuracy and consistency of the PINN model. This work highlights PINN's potential for hydraulic studies of host rocks in deep geological repository safety assessments, suggesting further exploration of complex structures, multi-physics coupling, uncertainty quantification, and larger-scale applications. Overall, this research shows the value and potential of PINN as a tool for studying coupled multiphysics processes in deep geological environments.

## References:

1. Tsang C-F, Bernier F, Davies C. Geohydromechanical processes in the Excavation Damaged Zone in crystalline rock, rock salt, and indurated and plastic clays—in the context of radioactive waste disposal. *International Journal of Rock Mechanics and Mining Sciences.* **2005**; *42* (1): 109-125. DOI: https://doi.org/10.1016/j.ijrmms.2004.08.003.

2. Birkholzer JT, Bond AE, Tsang C-F. The DECOVALEX international collaboration on modeling of coupled subsurface processes and its contribution to confidence building in radioactive waste disposal. *Hydrogeology Journal.* **2024**; *32* (5): 1295-1305. DOI: 10.1007/s10040-024-02799-7.

3. IAEA. *Geological Disposal Facilities for Radioactive Waste*; INTERNATIONAL ATOMIC ENERGY AGENCY, 2011.

4. Oehberg A, Rouhiainen P, Oy P. *Posiva Groundwater Flow Measuring Techniques*; Posiva Oy, 2000.

5. Neuman SP. Maximum likelihood Bayesian averaging of uncertain model predictions. *Stochastic Environmental Research and Risk Assessment.* **2003**; *17* (5): 291-305. DOI: 10.1007/s00477-003-0151-7.

6. Helton JC. Uncertainty and sensitivity analysis in performance assessment for the Waste Isolation Pilot Plant. *Computer Physics Communications.* **1999**; *117* (1): 156-180. DOI: https://doi.org/10.1016/S0010-4655(98)00171-4.

7. Wang S, Teng Y, Perdikaris P. Understanding and Mitigating Gradient Flow Pathologies in Physics-Informed Neural Networks. *SIAM Journal on Scientific Computing.* **2021**; *43* (5): A3055-A3081. DOI: 10.1137/20m1318043.

8. Raissi M, Perdikaris P, Karniadakis GE. Physics-informed neural networks for subsurface flow problems. *Journal of Computational Physics.* **2019**; *378*: 686-707. DOI: 10.1016/j.jcp.2018.10.045.

9. Oehberg A, Rouhiainen P, Oy P. Posiva Groundwater Flow Measuring Techniques. *Posiva Oy.* **2000**.

10. Raissi M, Perdikaris P, Karniadakis GE. Physics-informed neural networks: A deep learning framework for solving forward and inverse problems involving nonlinear partial differential equations. *Journal of Computational Physics.* **2019**; *378*: 686-707. DOI: https://doi.org/10.1016/j.jcp.2018.10.045.

11. He Q, Barajas-Solano D, Tartakovsky G, Tartakovsky AM. Physics-informed neural networks for multiphysics data assimilation with application to subsurface transport. *Advances in Water Resources.* **2020**; *141*: 103610. DOI: https://doi.org/10.1016/j.advwatres.2020.103610.

12. Yang L, Meng X, Karniadakis GE. B-PINNs: Bayesian physics-informed neural networks for forward and inverse PDE problems with noisy data. *Journal of Computational Physics.* **2021**; *425*: 109913. DOI: https://doi.org/10.1016/j.jcp.2020.109913.

13. Zheng T, Sun C, Zhang J, Ye J, Rui X, Wang Z. A multi-aggregator graph neural network for backbone exaction of fracture networks. *Computational Geosciences.* **2024**; *28* (3): 537-549. DOI: 10.1007/s10596-024-10281-2.

14. Amini D, Haghighat E, Juanes R. Physics-informed neural network solution of thermo–hydro–mechanical processes in porous media. *Journal of Engineering Mechanics.* **2022**; *148* (11): 04022070.

15. Selvadurai APS, Głowacki A. Estimates for the local permeability of the Cobourg limestone. *Journal of Rock Mechanics and Geotechnical Engineering.* **2018**; *10* (6): 1009-1019. DOI: https://doi.org/10.1016/j.jrmge.2018.07.002.

16. Paszke A, Gross S, Chintala S, Chanan G, Yang E, DeVito Z, Lin Z, Desmaison A, Antiga L, Lerer A. Automatic differentiation in PyTorch. 2017.

17. Gens A, Guimaraes LdN, Garcia-Molina A, Alonso EE. Factors controlling rock–clay buffer interaction in a radioactive waste repository. *Engineering Geology.* **2002**; *64* (2): 297-308. DOI: https://doi.org/10.1016/S0013-7952(02)00026-1.

18. Heaton J, Ian Goodfellow YB, and Aaron Courville:. Deep learning. *Genetic Programming and Evolvable Machines.* **2018**; *19* (1): 305-307. DOI: 10.1007/s10710-017-9314-z.

19. Comsol. COMSOL Multiphysics® 5.3. **2017**.